Numerical simulations of a fluidized granular flow entry into water: insights into modeling tsunami generation by pyroclastic density currents

L. Battershill [1,2], C. N. Whittaker[1], E. M. Lane [2], S. Popinet[3], J. D. L. White[4], W. L. Power[5], P. Nomikou [6]

[1]University of Auckland, New Zealand
[2]National Institute of Water and Atmospheric Research, 10 Kyle Street, Christchurch, New Zealand, 8011
[3]Sorbonne Université and CNRS, Institut Jean le Rond d'Alembert, UMR 7190, Paris, France
[5]GNS Science, 1 Fairway Drive, Avalon, Lower Hutt 5011, New Zealand
[4]University of Otago, 362 Leith Street, North Dunedin, Dunedin 9016, New Zealand
[6]University of Athens, Liviis 19, Zografou 157 71, Greece

Key Points:

- Numerical experiments of fluidized granular flows entering water are performed to study tsunamis generated by pyroclastic density currents.
- A fluidized granular flow modeled as a Newtonian fluid reproduces the complex flow-water interactions observed in laboratory experiments.
- The properties of the generated wave and resulting energy vary significantly with slope boundary condition and granular-fluid viscosity.

Corresponding author: Lily Battershill, `lbat537@aucklanduni.ac.nz`

Abstract

The tsunami generation potential of pyroclastic density currents (PDCs) entering the sea is poorly understood, due to limited data and observations. Thus far, tsunami generation by PDCs has been modeled in a similar manner to tsunami generation associated with landslides or debris flows, using two-layer depth-averaged approaches. Using the adaptive partial differential equation solver Basilisk and benchmarking with laboratory experiments, this work explores some of the important parameters not yet accounted for in numerical models of PDC-generated tsunamis. We use assumptions derived from experimental literature to approximate the granular, basal flow component of a PDC as a dense Newtonian fluid flowing down an inclined plane. This modeling provides insight into how the boundary condition of the slope and the viscosity of the dense granular-fluid influence the characteristics of the waves generated. Four interaction regimes are identified, which correspond to different granular-fluid Froude numbers and slope boundary conditions. Under certain conditions, the experimental physics is captured well in the numerical model, which validates the underlying assumption of Newtonian fluid-like behaviour in the context of wave generation. We show that the energy dissipation prior to breaking is a significant indicator of the far-field wave energy and amplitude. The results from this study also suggest the importance of considering vertical variation in inertia in wave generation models. Furthermore, we demonstrate that granular-fluids more dense than water are capable of shearing the water surface and generating significant amplitude waves, despite vigorous overturning.

Plain Language Summary

When a volcano erupts, it ejects large quantities of volcanic rock, ash and debris. These ejected materials can flow very rapidly down the side slopes of the volcano- these flows are called pyroclastic density currents (PDCs). When PDCs enter the sea, they displace water and can generate tsunami waves with enormous destructive potential. One method of understanding this potential is by mathematically modelling the flow and its interactions with water, and validating these model results again laboratory data. The present study compares numerical model results with laboratory experiments of PDC generated tsunamis, to understand how our assumptions about the flow and its motion along the boundary can affect the amount of energy transferred to the generated waves. We approximate a PDC generated tsunami as a dense fluid moving down a slope into water. The amount of friction on the slope and the properties of the dense fluid lead to different interactions between the PDC and the water, which we classify into four regimes. The regimes lead to a wide range of wave breaking behaviours. Our results show the importance of the boundary conditions and fluid properties in correctly capturing experimental observations and in predicting how PDCs generate tsunamis.

1 Introduction

1.1 Volcanic tsunamis

Around 80% of tsunamis are triggered by underwater earthquakes which cause a sudden and rapid displacement of the water surface. Due to the wavelengths associated with the large horizontal scale of the fault rupture (tens to hundreds of kms), this displacement results in long period waves capable of propagating across ocean basins (Center, 2006). Tsunamis can also be generated through sub-aerial and submarine landslides, meteorite impacts and volcanic eruptions. Volcanic eruptions themselves can generate waves through a number of mechanisms, including volcano-tectonic earthquakes, slope instabilities, PDCs, underwater explosions, shock waves and caldera collapse (Paris, 2015). There have been a number of geologically recent examples of such events. In 1996, the subaquatic explosive eruption near the northern shore of Karymskoye Lake in Kamchatka, Russia, generated multiple tsunamis (Belousov & Belousova, 2000). Locally to the source

($r < 1.3$ km), wave heights reached up to 30 m but were rapidly attenuated, leading to average runup heights of 2-3 m at locations 3 km from the source. Tsunamis generated by PDCs entering the sea were observed during the Montserrat 1997 and 2003 eruptions, with maximum run-up heights of 4 m in Montserrat (Narcisse et al., 2004), as well as the Rabaul 1994 eruption, where run-up heights reached 8 m in Rabaul Bay (Nishimura et al., 2000). The eruption of Krakatau volcano in 1883 triggered a tsunami that generated localized runup as high as 45 m and killed 36,000 people, understood to be as a result of voluminous PDCs entering the sea (Carey et al., 1996; Egorov, 2007).

Globally, around 20% of deaths associated with erupting volcanoes are a result of tsunamis generated directly by the eruption (Center, 2006). Despite the fact that over half of these deaths are thought to be a result of pyroclastic density currents (PDCs) entering the sea, the tsunami generation potential of PDCs is still poorly understood. Not only are there limited observations, but experimental as well as theoretical studies are rare, due to the complexities involved in the modeling and observations of such phenomena (Paris, 2015).

Both the potential impact and the probability of occurrence of these mechanisms are often not included in tsunami hazard assessments, which are most often primarily focused on earthquake generated tsunamis. Coastal communities living close to active volcanoes may be unprepared for the possibility of tsunamis generated by volcanic eruptions (Paris, 2015). A recent example of this is the December 2018 flank collapse of Anak Kraktau, Indonesia, which killed over 400 people. Although this event had been anticipated and modelled by Giachetti et al. (2012), mitigation strategies still do not take into account tsunami hazard potential associated with an erupting volcano (Syamsidik et al., n.d.).

1.2 Pyroclastic density currents

PDCs are density currents made up of volcanic rock, ash and debris. They are capable of transporting micrometer size ash particles to clasts larger than 1 m and can vary in temperatures from a few tens of °C up to 800°C (Sulpizio et al., 2014). These ground-hugging currents move at speeds up to 150 m/s down-slope away from their source (Legros & Druitt, 2000; Freundt, 2003) and exhibit runout lengths of 10^1-10^2 km (Cas et al., 2011). These properties make PDCs one of the most hazardous volcanic phenomena on Earth (Dufek, 2016; Lube et al., 2020). They form when hot mixtures of fragmented volcanic ash, rock and gas fail to become positively buoyant with respect to the surrounding air. Origins of PDCs include Plinian eruption column collapse (e.g. Sparks et al., 1978), breakup and collapse of effusing domes above volcanic slopes (e.g. Ui et al., 1999), inclined or laterally directed decompression jets (e.g. Belousov et al., 2007) and sustained pyroclastic fountaining (e.g. Báez et al., 2020). The eruption style responsible for generating the PDCs has effects on current concentration, rheology and steadiness.

A PDC behaves as a particle-driven gravity current, which entrains and intrudes into the colder and less dense atmosphere surrounding it (Lube et al., 2020). PDCs are often layered by density and lithofacies characterizations of PDC deposits are distinguished primarily by which of two layers dominates particle transport (Fisher, 1979; Dufek et al., 2015; Lube et al., 2020):

- PDCs comprising a dilute, fully turbulent upper layer with a thin and gas-pore-pressure-modified granular bedload region **(a dilute PDC).**
- PDCs comprising a dilute, fully turbulent transport regime overlaying a thick and gas-pore-pressure-modified granular flow regime **(a dense PDC)**.

Figure 1 illustrates these two end members. There is a broad spectrum of possible transport regimes between these two end members, as well as variations in velocity and temperature, making the flow dynamics hard to constrain. In some cases an intermediate regime (characterized by an inhomogeneous cluster-like distribution of particles)

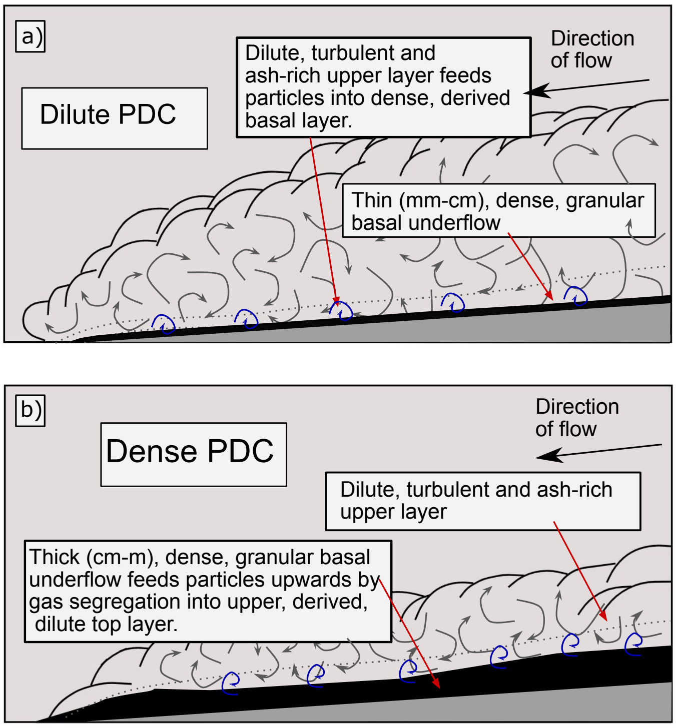

Figure 1. Diagram depicting the two key end members of PDC: (a) a dilute-type PDC and (b) a dense-type PDC. The present study focuses on the dense end member and ignores any momentum contribution from the dilute component.

governs the transition between the two layers (Lube et al., 2020). In other cases the boundary between the two regimes in a pyroclastic density current may be a relatively sharp interface, i.e. a steep density gradient (Branney & Kokelaar, 2005).

There are no direct observations of PDC interiors in the field, due to the hostile nature of the currents, the unpredictability of eruptive events and the dynamics of the events themselves (Baxter et al., 2005; Cas & Wright, 1991; Legros & Druitt, 2000). Experimental synthesis of PDCs, however, has recently revealed great detail on the internal dynamics of these currents and is pioneering work in PDC hazard assessment (Lube et al., 2020). Large scale experiments at the Pyroclastic flow Eruption Large-scale Experimental (PELE) facility simulate a gravitational collapse of an aerated suspension of natural volcanic particles. Recent laboratory experiments undertaken at this facility have demonstrated the existence of an air lubrication layer, which forms a near-frictionless region underneath the dense basal layer, helping explain the large run-out distances and high mobility observed in the field (Lube et al., 2019). The following section focuses on the ability of PDCs to generate tsunamis and outlines previous work on the subject including field studies and theoretical modeling, as well as numerical and experimental works.

1.3 Pyroclastic density current generated tsunamis: current understanding and previous works

Stratigraphic reconstruction, mapping of PDC deposits and observations of past events all suggest that in the past these currents have initiated tsunamis (e.g., Maeno & Imamura, 2011; Nishimura et al., 2000; Nomikou et al., 2016; Sulpizio et al., 2014; Waythomas & Watts, 2003). Geological investigation of sub-aqueous PDC deposits has concluded that when PDCs enter water they are generally disrupted explosively and/or ingest water and transform into water-supported mass-flows (e.g., Cas & Wright, 1991; Jutzeler et al., 2017; Carey et al., 1996).

Theoretical studies also assume that PDCs are capable of passing into, over or under the water. Watts (2003) argues theoretically that the most energetic and coherent water waves are produced by the dense, basal, granular flow component of the PDC, assuming that the violent dynamics of the splash zone or vertical ejection of debris at interaction have negligible effects on wave generation. Other phenomena such as steam explosions, flow pressure, shear, and pressure impulse were considered, but the authors conclude that these mechanisms would generate smaller waves. All previous numerical works, including the present study, accept this hypothesis and only consider the dense, basal component.

Laboratory experiments allow physical processes to be investigated in a controlled and (relatively) repeatable environment. This is particularly useful in the case of PDC modeling, where access to field data is limited. Furthermore, key parameters for numerical modeling must first be obtained from laboratory experiments. Freundt (2003) addresses the interaction of a PDC with water, but primarily focuses on thermodynamic behaviour in the flow-water interaction zone. A series of experiments is conducted, where granular flows of heated ignimbrite ash (20 - 400°C) and of bulk density near that of water, run down a smooth chute and enter a water-filled tank at an angle of 26°. For lower temperatures, the majority of material penetrates the surface and mixes with water, creating a forward-directed ash fountain, a turbulent mixing zone and a water-supported mass flow. As the temperature is increased, most of the flow is redirected across the surface of the water, mixing with water and generating steam explosions. No water-supported mass flow is generated in this latter case, but waves are generated as a result of steam explosions. Although waves were recorded during these experiments, their characteristics were not explored in detail.

More recent experiments on tsunami generation have pioneered research in the impact of cool, fluidized granular flows (representing the dense basal component of a PDC) into water and their effect on wave generation (Bougouin et al., 2020). Fluidized, micrometer spherical glass beads are released from a lock and are continually fluidized as they propagate down a ramp, before interacting with water. The fluidization is to replicate the high mobility and the interstitial gas pore pressure of dense PDCs observed experimentally (Lube et al., 2020) and in the field. Notable features of the mixing zone include the generation of a vertical granular jet, a leading wave and a turbulent mixing zone, similar to that observed by Freundt (2003). The vertical granular jet redirects a small amount of material across the surface of the water, while the remaining flow forms a gravity current on the slope. Spilling behaviour in the breaking wave is also observed. Their results suggest that it is sufficient to consider the fluidized granular flow as a single-phase fluid. The equivalent experiments were conducted using dense salt water flows and wave generation was similar to cases when fluidized grains were used.

Features of the leading wave in the near-field region are analyzed and it is concluded that in the case of fine-grained fluidized flows, the mass flux and volume of granular material are the primary parameters affecting the amplitude of the resulting wave. This is analogous to the findings from sub-aerial and submarine landslide literature, including Fritz et al. (2003) and the recent study by Robbe-Saule et al. (2020), which shows that the density has a second order effect on the wave amplitude.

Earlier experimental studies of tsunami generation by granular flows focus on initial parameters such as geometry and mass of an analog landslide (e.g., Fritz et al., 2003; Heller, 2009; Mohammed & Fritz, 2012). The work of Fritz et al. (2003) explores landslide generated impulse waves and the associated generation of hydrodynamic impact craters. It identifies three different regimes associated with the interaction zone and shows that the amount (and rate) of water displacement is governed by the slide Froude number (see Equation 1), the relative slide volume and the relative slide thickness (both with respect to the water depth). In the separated slide regime identified, a hydrodynamic impact crater forms, which is either outwards or backwards collapsing in nature.

Numerically modeling the interaction of a PDC with water and the resulting wave generation relies upon many simplifications. This includes approximating the density stratification and flow dynamics, as well as the sub-aqueous transport of the flow following its initial entry to the water. Previous numerical studies (e.g., Maeno & Imamura, 2011; Nomikou et al., 2016) of PDC generated tsunamis assume the dilute component of a PDC to be negligible in terms of its effect on wave generation and focus on the dense, basal layer. Generally, these studies utilise depth-averaged approaches when considering both the PDC and the water (where vertical inertia is ignored). Direct numerical simulation (DNS) can be used to capture the more complex physical processes occurring, but has been avoided in simulations of tsunami generation by PDC, primarily for computational efficiency when considering large scales. Capturing these physical processes is, however, a desirable next step towards improving our understanding of this phenomenon and improving the capabilities of present hazard assessment models.

1.4 Context of present study

Modeling and predicting the behaviour of granular flows remains a challenging goal, since granular flows are characterized by a large diversity of behaviours depending on their environment and conditions (Lagrée et al., 2011). Creating a generic continuum granular rheology is still very much an active area of research, challenges including the identification of a relevant variable to describe the transition from arrest to flow and the understanding of non-local effects. A PDC adds further complexity, with basal friction effects and transient pore pressure complicating the modeling further (Breard et al., 2020). Lube et al. (2020) also note that the vertical velocity profile remains somewhat parabolic as well as transient. Furthermore, the velocity at the slope boundary is not necessarily zero and there is a broad range of velocity configurations within these currents.

The present study numerically models the interaction of a laboratory-scale dense PDC with water and the associated waves generated using a high resolution two-dimensional numerical model, in order to investigate the potential of our model to capture some of the more complex physical processes occurring. This enables us to determine some of the key parameters involved in capturing the important physics. The definition of a boundary condition for the slope, in particular, is non-trivial. Our numerical study replicates the laboratory experiments of Bougouin et al. (2020), comparing with their experimental results to validate the numerical simulations. Bougouin et al. (2020) propose that the granular flow can be approximated as a dense, single-phase fluid, which is a useful assumption to make numerically in terms of simplifying the granular continuum rheology. Our numerical model is a useful means of testing this assumption. The modeling is achieved by numerically solving the Navier-Stokes equations on an adaptive grid, using the Basilisk flow solver (Popinet, 2021). Hereafter, the term *granular-fluid* refers to the dense granular flow, modelled as a Newtonian fluid.

The numerical simulation outputs show a strong agreement with the experimental results. Figure 2 shows a direct comparison for different times, for two initial column heights and resulting granular-fluid Froude numbers. The Froude number for the granular-fluid is defined as:

$$Fr = \frac{u_f}{\sqrt{gH_i}} \tag{1}$$

where u_f is the depth averaged u_x velocity over the height of the granular-fluid front at impact (or in the case of the laboratory experiments, the calculated front velocity), H_i is the initial water depth and g is the the gravitational acceleration. In the numerical snapshots, we present two-dimensional vertical slices at the scale of the laboratory domain. The red represents the granular-fluid, the yellow the water and the blue the air. Features of interaction including the generation of a granular jet, a plunging breaker and the retardation of the granular-fluid upon interaction with water are all captured in the numerical model. A characterization of interaction regimes is discussed in Section 3.2

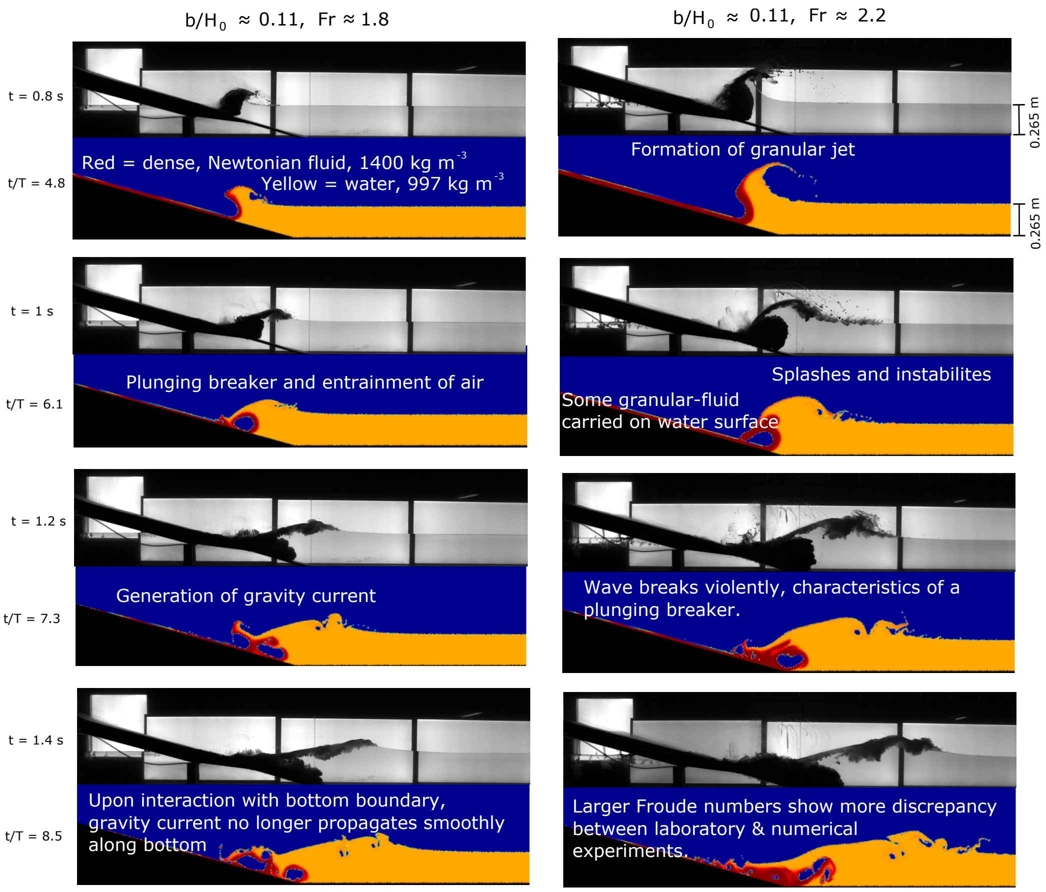

Figure 2. A comparison between numerical and experimental results (Bougouin et al., 2020), at four different times. The initial column heights in the experiments are 22.5 *cm* and 42.5 *cm* in the left and right columns, respectively. The numerical heights are initialized at 3 *cm* lower, to account for the residual grains left in the reservoir. The resulting Froude numbers are 1.8 and 2.2 in the left and right columns, respectively. More details on the setup information and outputs are discussed in methodology, Section 2.

and a detailed discussion of the experimental/numerical comparison is presented in Section 3.3. The strength of agreement between the numerical results and the experiments presented is remarkable, but this is highly sensitive to the boundary condition. Hence, the present study also investigates the effect of variability in the the granular-fluid viscosity and boundary condition of the slope (i.e. the boundary friction) on the vertical (perpendicular to the slope) x velocity profile of the granular-fluid, u_x, the wave generation process and the resulting far-field wave characteristics. A range of granular-fluid viscosities and boundary conditions is explored and a detailed characterization of the associated granular-fluid/water interaction regimes is presented. Furthermore, we investigate how different boundary conditions and associated regimes show different efficiencies of energy transfer from the granular-fluid to the water and the far field wave. We first outline the methodology used, followed by an extensive discussion and presentation of our results in the following section.

2 Methodology

The following sections outline our numerical methodology. Section 2.1 gives the assumptions made and the governing equations solved, Section 2.2 provides details of the Basilisk flow solver and the numerical setup and Section 2.3 discusses the outputs analyzed.

2.1 Assumptions made and governing equations solved

We assume the fluidized grains from the experiments of Bougouin et al. (2020) to behave as a continuum. This takes the form of a dense, viscous and incompressible Newtonian fluid. The dense fluid and the water are assumed to be miscible with one another, but immiscible with air, separated by a sharp interface. Surface tension is assumed to have negligible effect on interaction dynamics and wave propagation, due to the contrast of scales.

These assumptions lead to the applicability of the variable-density, multi-phase (VoF), incompressible Navier-Stokes equations:

$$\partial_t \mathbf{u} + \nabla \cdot (\mathbf{u}\mathbf{u}) = \frac{1}{\rho}\left[-\nabla p + \nabla \cdot (\mu(\nabla \mathbf{u} + \nabla \mathbf{u}^T))\right] + \mathbf{g} \tag{2}$$

$$\nabla \cdot \mathbf{u} = 0 \tag{3}$$

$$\partial_t f + \mathbf{u} \cdot \nabla f = 0 \tag{4}$$

$$\partial_t \tau + \mathbf{u} \cdot \nabla \tau = 0 \tag{5}$$

with p, $\mathbf{u}$, μ, ρ and $\mathbf{g}$ representing the pressure field, velocity field, dynamic viscosity, density and acceleration due to gravity respectively. f is the volume fraction tracer in our VoF approach that delineates between air ($f = 0$) and the variable density fluid ($f = 1$). The variable density fluid consists of the fluidized granular flow ($\tau = 1$) and the water ($\tau = 0$). Both the density ρ and the viscosity μ are therefore functions of τ and f, i.e. $\rho = \rho(\tau, f)$ and $\mu = \mu(\tau, f)$. The method described is an alternative to an immiscible three-phase approach, where three fluids are separated by an interface (e.g., Joubert et al., 2020).

The recent discovery of a low friction basal layer by Lube et al. (2020) highlights the importance of exploring a range of friction (boundary) conditions within our numerical model for the granular-fluid. We therefore use a Navier-slip boundary for the slope boundary condition, viz.,

$$u_t + b\frac{\partial u_t}{\partial z} = 0 \tag{6}$$

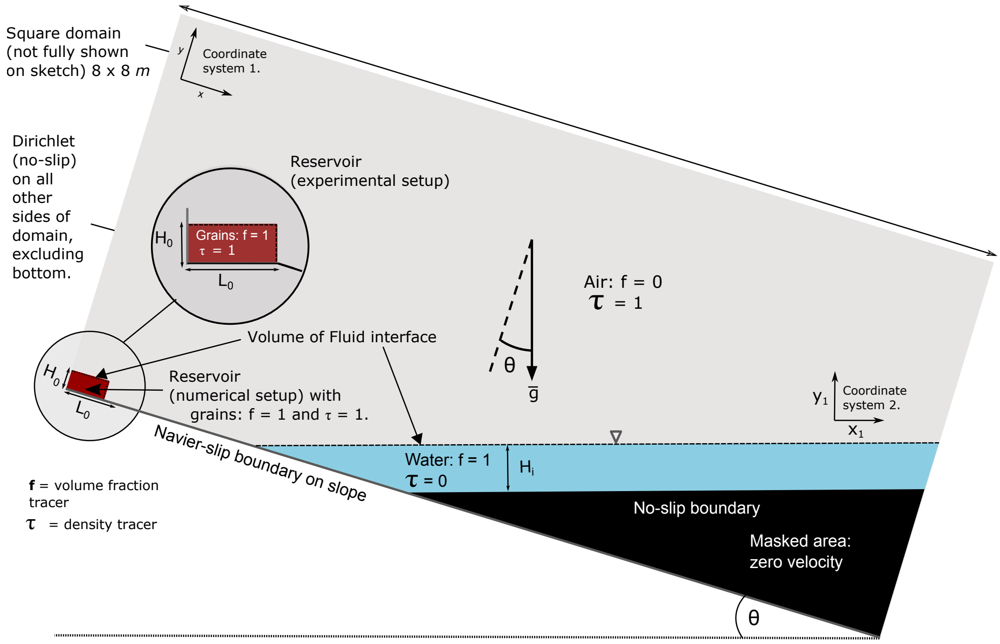

Figure 3. Setup of the initialized numerical domain, labelling the boundary implementations, tracer initialization and reference heights. The circular inset highlights the difference between the experimental reservoir and the Basilisk initialization.

where b represents the Navier slip length of the granular-fluid. The choice of this Navier-slip length allows us to vary this boundary condition between no-slip, partial-slip and free-slip.

2.2 Numerical implementation

These equations are solved using the adaptive partial differential equation solver Basilisk (Popinet, 2021), developed as the successor to Gerris by the same authors (Popinet, 2003, 2009, 2015). In Basilisk, an adaptive tree-grid structure is implemented which facilitates local refinement and coarsening, for computational efficiency. The Navier-Stokes solver has been successfully used in a number of two-phase problems to model splashing (Thoraval et al., 2012) and wave breaking in both two and three dimensions (Deike et al., 2015). A two-phase Volume of Fluid (VoF) approach is used to capture the interface between the air and the variable density fluid (Hirt & Nichols, 1981). The momentum equation is solved using the Bell Colella Glaz projection method (Bell et al., 1989), and we develop the momentum-conserving scheme for VoF advection to account for variable density on the water/granular fluid side of the VoF interface. Basilisk uses a conservative, non-diffusive, geometric VoF scheme (Scardovelli & Zaleski, 1999).

In the present study we consider a two-dimensional vertical slice. This will lead to the generation of more coherent vortical structures, which has implications when considering wave breaking and overturning that must be considered. Since Basilisk works primarily with square or cubic domains, the length of the domain L is set to be 8 m and the domain is rotated by angle $\theta = 15°$, to represent the slope (see Figure 3). This is in order to capture the dimensions of the experimental setup, see Bougouin et al. (2020) for details. This rotation of the domain leads to the definition of two coordinate systems; x, y before rotation (where x is in the downwards direction of the slope, with y perpendicular) and x_1, y_1 after rotation. The bottom of the tank is implemented by masking the equivalent part of the numerical domain (i.e. setting the normal and tangential velocity components of each grid cell to zero).

A maximum grid resolution of 4096^2 is used, leading to a minimum cell size of $L/4096$ $\approx 1.4\ mm$. We conduct a convergence test, showing that this grid-size enables the adaptive mesh refinement to accurately solve for the interface and the vortical structures. This implementation ensures the maximum grid resolution is maintained at the VoF interface.

In order to compare our results with the experiments of Bougouin et al. (2020), it is necessary to determine the parameters most representative of the experimental setup. The maximum density of the granular fluid is set to 1400 kgm^{-3} and the density of the water is 997 kgm^{-3}. We have no information on the equivalent dynamic viscosity of the dense granular-fluid and the boundary condition on the slope in the experimental setup, since these conditions are non-trivial to define. Section 3 therefore presents an exploration of this parameter range (and the associated granular-fluid velocity profiles) in order to determine the most representative conditions and to explore how these parameters control granular-fluid/water interaction dynamics. Although computationally intensive to solve the full Navier-Stokes equations, this validation gives us a benchmark against which to check depth-averaged or multi-layer approaches (e.g., Audusse, 2005; Popinet, 2020).

The Navier-slip boundary condition is set along the bottom x boundary (i.e. the slope). For the implementation of the tank bottom, the velocity field is set to zero at all time-steps, leading to a no-slip (Dirichlet) boundary condition, as depicted by the shaded black area in Figure 3. This implementation is limited by the current capabilities of embedded boundaries in Basilisk, however the primary focus of our analysis is associated with initial wave generation and propagation before the current interacts with the bottom boundary. The vertical u_x profile of the granular-fluid is dependent on the granular-fluid viscosity and boundary condition. The boundary-layer thickness (denoted in Figure 4 by δ_x) represents the distance normal to the wall to a point where the velocity of the granular-fluid has reached a certain percentage of the outer velocity u_{max}, e.g. 99%. (Schlichting & Gersten, 2016). There is no unique boundary–layer thickness, since the effect of the viscosity in the boundary layer decreases asymptotically as we move outwards from the wall.

2.3 Outputs

Following Bougouin et al. (2020), we evaluate the front height h_f and output the front velocity profile $u_{x,front}$ at 10 cm from the head of the granular-fluid at the time of impact (i.e. 10 cm from the slope-water intersection). The constant front velocity u_f is defined in our numerical experiments as the depth-averaged velocity at this location.

We also consider the energy of the system. We calculate the total energy:

$$E = E_k + E_g \tag{7}$$

as the sum of gravitational potential energy;

$$E_g = \int \rho g y dx dy - E_{rest} \tag{8}$$

and the kinetic energy:

$$E_k = \frac{1}{2} \int \rho u^2 dx dy \tag{9}$$

for the granular-fluid, water and air. The components are calculated at each location using the respective volume fraction f and granular-fluid tracer τ values. At initialization, the kinetic energy is 0 and the total energy of the domain is stored in the po-

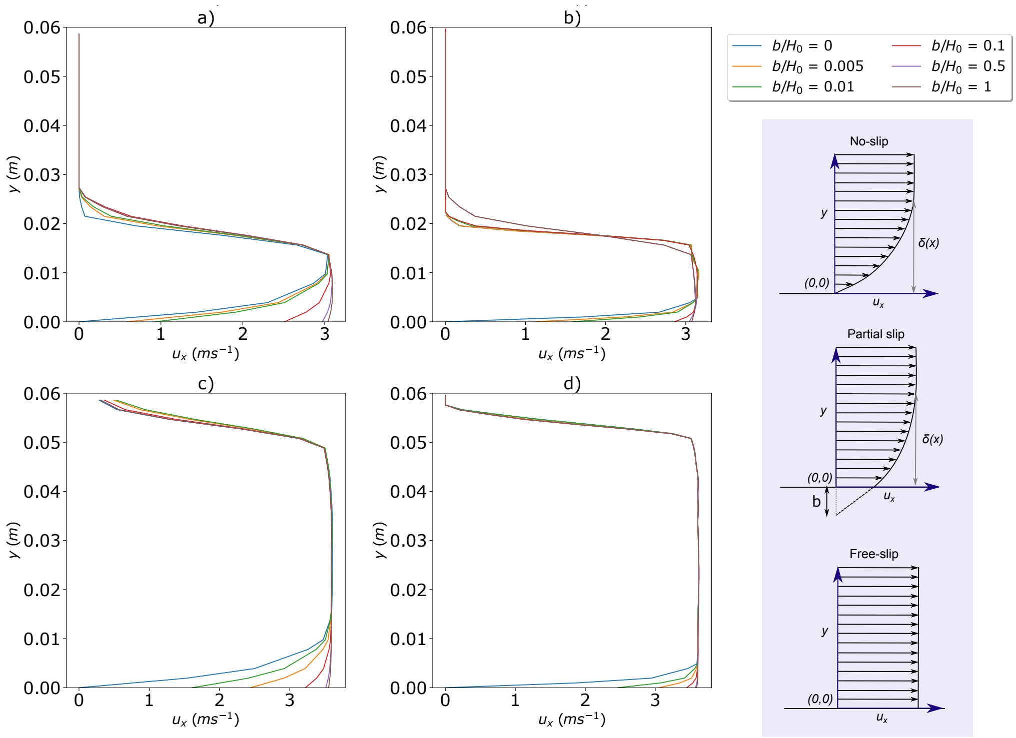

Figure 4. Velocity profiles of the granular-fluid (10 cm from the head) at the time of impact, for a range of dimensionless slip lengths b/H_0. a) $H_i = 18.5\ cm$, $\mu = 0.1\ Ns/m^2$, b) $H_i = 18.5\ cm$, $\mu = 0.01\ Ns/m^2$, c) $H_i = 39.5\ cm$, $\mu = 0.1\ Ns/m^2$, a) $H_i = 39.5\ cm$, $\mu = 0.01\ Ns/m^2$. Light blue inset shows how boundary conditions on the slope affect the boundary layer thickness $\sigma(x)$ at a time t. Graphical depiction of slip length b. $b = 0$ for no-slip and $b = \infty$ for free-slip.

tential energy of the granular-fluid, i.e. $E_{init} = E_{g,init}$. The constant E_{rest} in the gravitational potential energy equation is introduced to define a zero potential energy for an unperturbed surface, including the submerged granular-fluid at rest.

3 Results

3.1 Vertical profiles of the horizontal velocity component of the granular-fluid, at interaction

Figure 4 shows the vertical profiles of the horizontal velocity component of the granular-fluid at impact (the time-step at which the granular-fluid first interacts with the water) as we vary the boundary between the no-slip and free-slip end members. Velocity profiles are shown for two different values of dynamic viscosity: 0.01 Ns/m^2 and 0.1 Ns/m^2, for $H_0 = 18.5\ cm$ and $H_0 = 39.5\ cm$. The dimensionless slip length is defined as: b/H_0, where H_0 is the initial column height.

For a given dynamic viscosity μ and given column height H_0, the thickness of the boundary layer h_b at impact remains approximately the same for all values of slip length b, whereas the depth averaged velocity across the flow front u_f is highly dependent on b. As the dynamic viscosity of the granular flow increases, the boundary layer thickness h_b increases. As the initial column height H_0 increases, h_f at impact also increases, but only a small increase of h_b is observed. For higher dynamic viscosities and lower initial

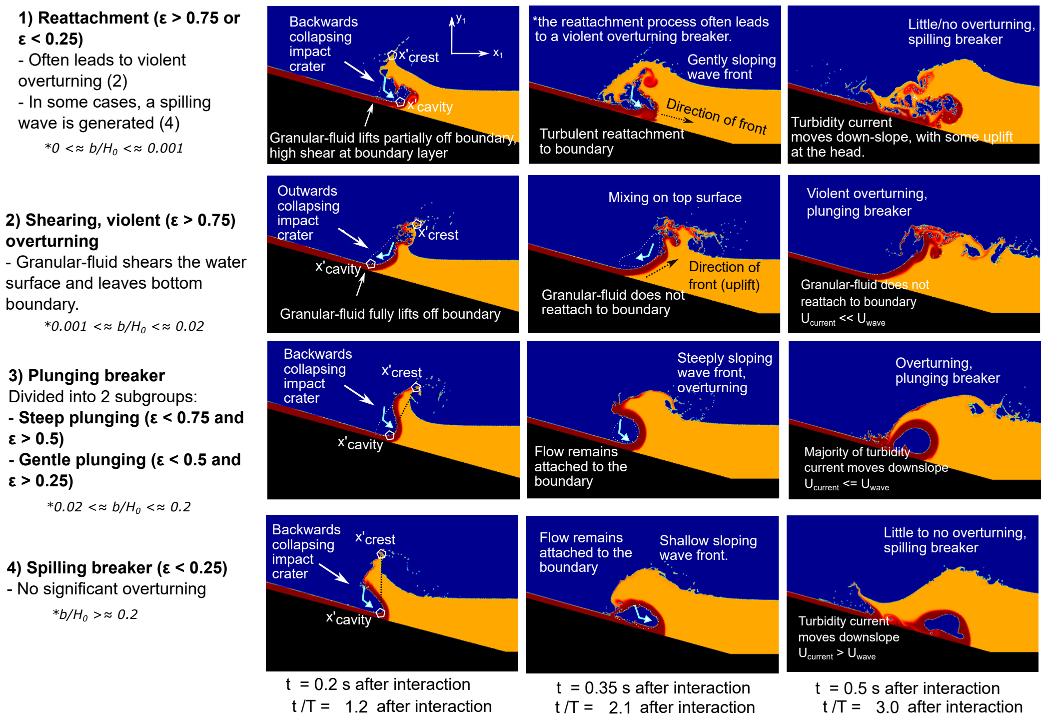

Figure 5. Regime *1*: Turbulent granular-fluid reattachment, spilling or violently overturning breaker. Regime *2*: Granular-fluid shearing, violent overturning, plunging breaker. Regime *3*: Partial granular-fluid attachment, overturning, plunging breaker. Regime *4*: Full granular-fluid attachment. Spilling breaker, little/no overturning. These snapshots are for the initial conditions $\mu = 0.1\ Ns/m^2$ and $H_i = 18.5\ cm$. * The b/H_0 values shown are specific to these initial conditions leading to Fr = 1.8, although the same regimes are observed across a range of Froude numbers.

column heights (i.e. $\mu = 0.1\ Ns/m^2$, $H_0 = 18.5\ cm$), we observe a well−resolved boundary layer, as shown in Figure 4. As dynamic viscosity is reduced (i.e. $\mu = 0.01\ Ns/m^2$), a higher resolution (8192^2) is required to resolve a similar number of grid cells over the boundary layer.

3.2 Snapshots and evaluation of interaction regimes

The dense fluid-water interaction shows four different regimes, which are illustrated in Figure 5. Each row represents a different interaction regime, which depends on the slip length b, initial column height H_0 and the granular-fluid viscosity. The regimes depicted are present across the range of column heights and dynamic viscosities considered.

The interaction regimes are differentiated by the amount of granular-fluid directed across the water surface versus down-slope, the type of impact crater generated and the leading wave characteristics. A quantitative description of the breaking regimes is developed, which refers to a steepness parameter ϵ, which is defined as:

$$\epsilon = (x_{1,crest,t'=0.2s} - x_{1,cavity,t'=0.2s})/H_0 \tag{10}$$

where $x_{1,cavity,t'=0.2s}$ refers to the x_1 position of the cavity (the impact crater) at time $t = 0.2$ s after interaction and $x_{1,crest,t'=0.2s}$ is the x_1 position of the wave crest. ϵ describes the offset between the head of the gravity current and the wave crest and is depicted graphically by the dashed black line in Figure 5. A larger positive offset results in a steeper wave, increased overturning and a larger value of ϵ. The breaking characteristics are described by the amount of overturning of the free surface. A spilling breaker is defined as a breaking wave with no significant overturning or entrainment of air. A plunging breaker exhibits overturning of the free surface, which can vary in steepness.

In regime *1*, the granular-fluid front is initially redirected across the surface of the water, leaving the bottom boundary. This reattachment can occur at a number of times after the initial interaction, which affects the type of wave generated.

In some cases, reattachment occurs rapidly and a gravity current is generated which, while on the slope, moves at a similar velocity to that of the leading wave. In this situation, the velocity and directionality of the granular-fluid front mean that the majority of the fluid momentum is directed down-slope, leading to the generation of a backwards collapsing impact crater (as depicted in Figure 5), similar to what is observed and described in the landslide tsunami generation experiments conducted by Fritz et al. (2003). Under these conditions, $\epsilon < 0.25$. The impact crater is governed by a surface closure resulting in the inclusion of air pockets in the form of a cavity. During this interaction, a small jet is formed at the crest and a spilling wave is generated. The initial upwards direction of momentum followed by turbulent reattachment of the granular-fluid appears to slightly retard the flow.

In other cases, the majority of the granular-fluid is directed across the water surface. Reattachment is also observed within the first 0.2 s after impact, but in these cases violent overturning and mixing at the interaction zone are prevalent. This interaction style does not support the generation of a gravity current and most material therefore remains near the interaction zone. In these cases, $\epsilon > 0.75$. Regime *1* therefore refers to reattachment behaviour, but the wave breaking style associated with this regime can vary. For this reason, is important to note that while ϵ is used to characterise the wave steepness, for a full characterization of regime *1* both a qualitative and quantitative approach is required.

In regime *2*, the granular-fluid is transported both upwards and outwards at interaction and shears the surface of the water, leaving the bottom boundary almost entirely. The majority of momentum is redirected across the water surface (depicted by the blue arrows in 5). The collapse behind the leading wave is, in this regime, referred to as an outwards collapsing impact crater. In contrast to the backward collapsing impact crater, no water surface closure behind the wave front is observed in this case and the collapse occurs through water rushing back towards the ramp under the influence of gravity (Fritz et al., 2003). This regime does not support the generation of a gravity current and most material therefore remains near the interaction zone. The wave dynamics in this regime can be described by a steep plunging breaker which leads to violent overturning, with splashes, liquid droplets and gas bubbles formed when the overturning wave impacts upon the liquid. In this regime, $\epsilon > 0.75$.

In regime *3*, some granular-fluid is also expelled upwards and outwards at interaction, redirecting some momentum across the water surface, but the majority of the granular-fluid remains attached to the bottom boundary. This behaviour leads to the generation of a plunging breaker, with less significant mixing and overturning observed than for regime *2*. A backwards collapsing impact impact crater is formed in this regime. It is observed that the steepness of the wave generated (and the respective amount of overturning) is determined by the relative proportion of momentum directed across the surface versus down-slope. As less granular-fluid is directed across the water surface, the granular-fluid penetrates the water more rapidly leading to a shallower wave front. Some overturning and the entrainment of gas bubbles is observed, but we do not observe significant splashing. Direct numerical simulation (DNS) of steep plunging breakers has been performed by Deike et al. (2015) and show similar dynamics to that described in the present study.

In this regime, a steeply plunging breaker is defined as $0.5 < \epsilon < 0.75$. A gently plunging breaker is associated with the range $0.25 < \epsilon < 0.5$.

Finally, in regime *4* the granular-fluid appears to initially expel the water upward, then punches through the water, forming a backwards collapsing impact crater. This regime displays similar characteristics to the spilling breaker generated in some reattachment cases associated with regime *1*, although the granular-fluid remains permanently attached to the bottom boundary. Initial uplift evolves into a leading wave, which does not appear to exhibit significant breaking, although some spilling is observed. Overturning is not apparent at the scales considered. A gravity current is generated which initially moves at a greater velocity to that of the leading wave.

As we change the dynamic viscosity or the initial column height within the range of parameters considered, qualitatively similar regimes are observed. For each viscosity and column height, the change in regimes generally follows the same pattern as the dimensionless slip length b/H_0 is increased (*1*, in some cases, followed by *2*,*3*,*4*). The values of b/H_0 corresponding to the transition between regimes differ depending on the Froude number of the granular-fluid (see Equation 1). In many cases (in particular as Froude number is increased), the no-slip condition ($b/H_0 = 0$) will not lead to granular-fluid reattachment and instead the interaction will display characteristics similar to regime *2*.

3.3 Experimental comparison

Qualitatively, we compare snapshots from the experimental results of Bougouin et al. (2020) with the outputs from our numerical simulations. Not only does comparison with experimental snapshots provide confidence that our numerical solver is capturing accurate physics, but it allows us to make inferences about the important parameters controlling the wave generation.

In the experimental snapshots (Bougouin et al., 2020), the details of the interaction behind the granular-fluid front (i.e. the hydrodynamic impact crater) cannot be observed due to vigorous mixing of the granular material. However, a number of key features associated with the wave generation, the granular-fluid separation and the propagation of the gravity current are identified. As the granular-fluid impacts water, some momentum is directed across the water surface, causing the generation of an outwards projecting granular jet. This behaviour is reported in the cool volcanic ash experiments of Freundt (2003). The majority of the granular-fluid undergoes mixing and forms a water-supported mass flow which travels down-slope, at a slower velocity to that of the leading wave. For experimental Froude numbers > 2.0 (see Equation 1 for definition), the wave generated in the initial 0.4 seconds after interaction displays features of a steeply plunging breaker. As the Froude number decreases, the plunging breaker becomes more gentle and for low Fr (Fr ≈ 1.6), a spilling breaker is generated. It cannot be observed whether or not a reattachment process occurs.

The plunging breaker behaviour is also observed in our numerical results (regime *3*), where granular-fluid splitting leads to the generation of a steep/gently plunging breaker and the formation of a gravity current. These results and observations imply that in the context of the physical experiments, the flow fluidization and associated boundary behaviour play an important role in determining the interaction dynamics, by determining the distribution of granular-fluid momentum at impact.

Given the parameter range we choose to explore in the present study, we can make inferences about the most representative conditions of the laboratory setup. The experimental results cover a range of Froude numbers comparable to our numerical experiments, but we have limited information surrounding the friction condition. Combining our insights from Figures 4 and 5, we infer that the experimental granular flow displays boundary behaviour similar to a mixed boundary condition. Figure 2 shows how the numerical results capture the generation of the jet, the plunging breaker behaviour with associated splashes and overturning, as well as the approximate shape and velocity of the gravity current in the first 1.2 s. For the case where $Fr \approx 2.2$ (the right column), the numerical results show increased overturning for later times in comparison to the experimental snapshots. Furthermore, after ≈ 1.2 s, the gravity current no longer propagates along the bottom boundary. For the same initial column height, the granular-fluid in the numerical setup moves faster than the equivalent laboratory experiments (most likely a result of the difference in gate initialization), leading to a higher amplitude wave. The lift observed from the bottom boundary (of the tank) in our numerical experiments is likely a result of the bottom boundary implementation, which is limited to no-slip. As shown in the interaction of the granular-fluid with water for no-slip conditions, granular-fluid lift from the bottom boundary is often observed. Despite these observations, the wave generation in the first 1.2 s appears qualitatively similar and the propagation and shape of the leading wave are well captured. These observations suggest that the fluidization process results in a reduction in friction, but the bottom boundary is not entirely frictionless. It also suggests that a small change in boundary condition can lead to a significant change in interaction behaviour. The results also validate the assumption that a Newtonian fluid can be used as an approximation for a fluidized granular flow, particularly in the context of wave generation.

In the high temperature experiments of Freundt (2003), all of the granular-fluid is redirected across the surface of the water, leading to violent overturning, similar to what is observed in regime *2*. Smaller amplitude and localized waves are observed, which are associated with steam explosions occurring near the surface of the water. Although temperature is not considered in our numerical simulations, we observe a similar interaction behaviour in regime *2*, whereby the granular-fluid is redirected across the surface of the water, leading to violent breaking behaviour. This granular-fluid redirection can be attributed to a number of potential factors, including changes in density or buoyancy, boundary behaviour and shear. The present study does not explore the effects of temperature, but this is an interesting area for future research.

3.4 Wave properties post-interaction

3.4.1 Energy evolution and transfer

It has been demonstrated across multiple experimental and numerical studies (e.g., Deike et al., 2015) that wave breaking has a significant effect on energy dissipation and momentum transfer. For breaking waves on a flat bottom, the steeper the wave and the more overturning observed, the greater the energy dissipation. In our numerical simulations there are a number of significant dissipation processes occurring including, but not limited to, the wave breaking; the collapse of the hydrodynamic impact crater and air entrainment at the mixing zone. In the case where a shallower wave is observed and less dissipation would be expected due to the wave breaking (for some of the high slip conditions, no breaking is observed), there may be increased dissipation elsewhere in the domain; i.e. in the impact crater collapse or the propagation of the gravity current. Similarly, in the case of violent overturning there is no significant impact crater collapse or propagation of a gravity current. For this reason, beyond the initial granular-fluid propagation and wave generation, differentiating between different energy dissipation mechanisms is non-trivial. Exploring the energy evolution of the domain (and its components) does, however, allow us to determine the amount and timing of energy dissipation associated with the different boundary conditions and the relative granular-fluid/water interaction regimes, providing a more quantitative view on the descriptions of the different regimes. Understanding the relationship between the wave generation regimes and energy transfer from the granular-fluid to the water allows us to to explore our parameter space in greater detail and expand on what is achievable in the laboratory. Detailed data describing the evolution of the granular-fluid and its velocity profile, as well as the energy transfers from the granular-fluid to the water are not available from the laboratory experiments.

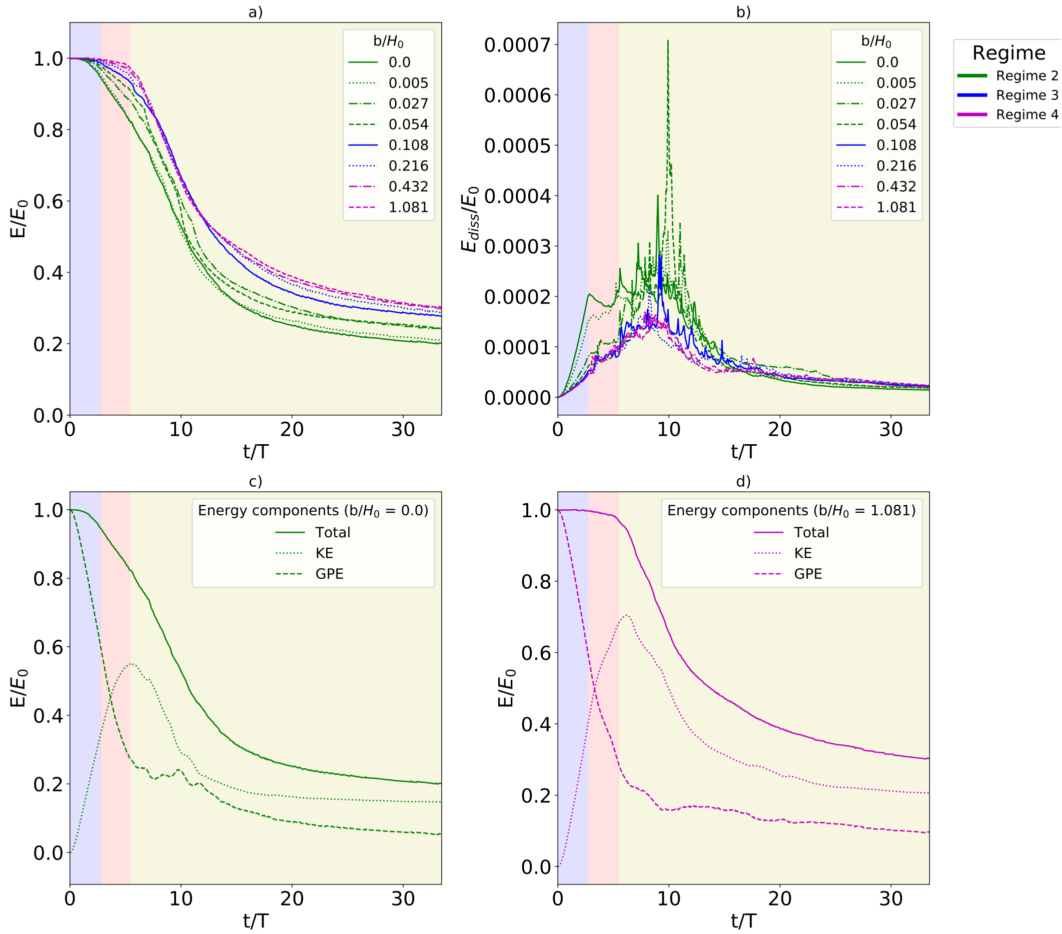

Figure 6. a) Normalized total energy of domain as a function of time t/T (where $T = H_i/\sqrt{(gH_i)}$, for a range of slip lengths b/H_0. b) Energy dissipation rate (relative energy lost per T) of entire domain as a function of time t/T. c) and d) Normalized total energy of domain, including the normalized gravitational and kinetic components as a function of time t/T. Each graph represents a different slip length, with the lines colored according to the breaking style or regime that slip length identifies with c) $b/H_i = 0.0$ and d) $b/H_i = 1.081$. The background colors broadly represent the different stages of the simulation: purple = granular-fluid propagation on slope, pink = initial wave generation and yellow = wave breaking and impact crater collapse.

Figure 6 shows a) the normalized evolution of the total energy of the domain and b) the dissipation rate for a range of slip lengths b/H_0, for the initial condition where $H_0 = 18.5\ cm$ and $\mu = 0.1\ ms^{-2}$. This is for illustration purposes, since this initial condition is associated with the most significant impact of the boundary condition on the u_x velocity profile of the granular-fluid (see Figure 4). The lines are colored by the breaking regime that the slip length leads to. Figure 6c and 6d present the evolution of the normalized total energy of the domain, along with the gravitational and potential components, for $b/H_0 = 0.0$ and $b/H_0 = 1.081$, plots c) and d) respectively. Figure 7 presents the kinetic, potential and total energy evolutions for the granular-fluid and the water components, including their dissipation rate.

As the granular-fluid propagates down the slope, the total energy of the domain begins to decrease. This decrease is greater for high friction cases (i.e. smaller values of b/H_0) and is most clearly depicted in the total energy dissipation plot (Figure 6b), which shows the increased dissipation rate for high friction conditions during the initial propagation. Figure 7h shows that the dissipation occuring at this stage is driven by the granular-fluid. Figures 6c and 6d show the transfer of potential energy to kinetic energy at this stage, as the granular-fluid propagates down-slope. Figure 7 confirms that this energy transfer is contained in the granular fluid.

As the granular-fluid impacts the water and the water surface is uplifted (as depicted in Figure 5, $t/T = 1.2$ after interaction), the total energy of the domain continues to decrease for all regimes. At the transition between uplift and the onset of wave breaking (and/or impact crater collapse), the kinetic energy of the domain and the kinetic energy of the granular-fluid reach a maximum for all regimes and the rate of change in potential energy decreases, as the granular-fluid slows down within the collapsing region (i.e. Figure 5, $t/T = 2.1$ after interaction). For regime 2, the potential energy of the granular-fluid remains higher than for other regimes: a result of the fluid shearing across the water surface. The maximum value of total kinetic energy observed is ≈ 20 % higher for lower friction conditions (i.e. $b/H_0 = 1.081$), since in these cases less energy has been dissipated in the initial propagation and interaction stages. Once wave breaking starts and/or the impact crater collapses, the granular-fluid is slowed and the kinetic energy of the granular-fluid decreases abruptly, which corresponds with a decrease of the total energy in the domain. However, during this stage, the total energy of the water and its components continue to increase. Generally, the dissipation rate at this stage increases as the amount of overturning increases in the wave breaking and entrainment of air at the shoreline during the impact crater collapse.

The total energy of the water reaches a maximum at $t/T \approx 10$ and is greatest for lower friction conditions. The time of maximum energy in the water corresponds to the time at which the dissipation rate of the granular-fluid begins to slow, and the potential energy of the granular-fluid flattens, suggesting that the grains stop imparting significant energy to the water at this stage. The dissipation rate for the water associated with $b/H_0 = 0$ decreases most rapidly. It can be observed that after $t/T \approx 30$, the energy dissipation rates for all slip conditions begin to tend towards a steady rate, as breaking ceases and the granular-fluid has undergone significant mixing.

For later times (i.e. $t/T > 30$), the total energy of the water tends towards a more constant value. When considering tsunami generation potential, this observation suggests that the wave is carrying sufficient energy to propagate significantly further, without considerable dissipation, if it were to continue in an infinite domain. Generally, the total energy of the water is greatest for lower friction conditions, with a few exceptions where an increase in total energy is observed for regimes *2* or *3* at $t/T \approx 20$. We hypothesize this to be a result of granular-fluid propagation: in these cases, inferences from both snapshots and energy evolution plots demonstrate that the granular-fluid remains attached (or reattaches) to the bottom boundary, thus imparting more energy to the water in the near-field than simulations where the granular-fluid lifts off the tank bottom. This suggests that energy plots for the separate components, when considering the entire domain, cannot tell us all the information about the far-field wave if the gravity cur-

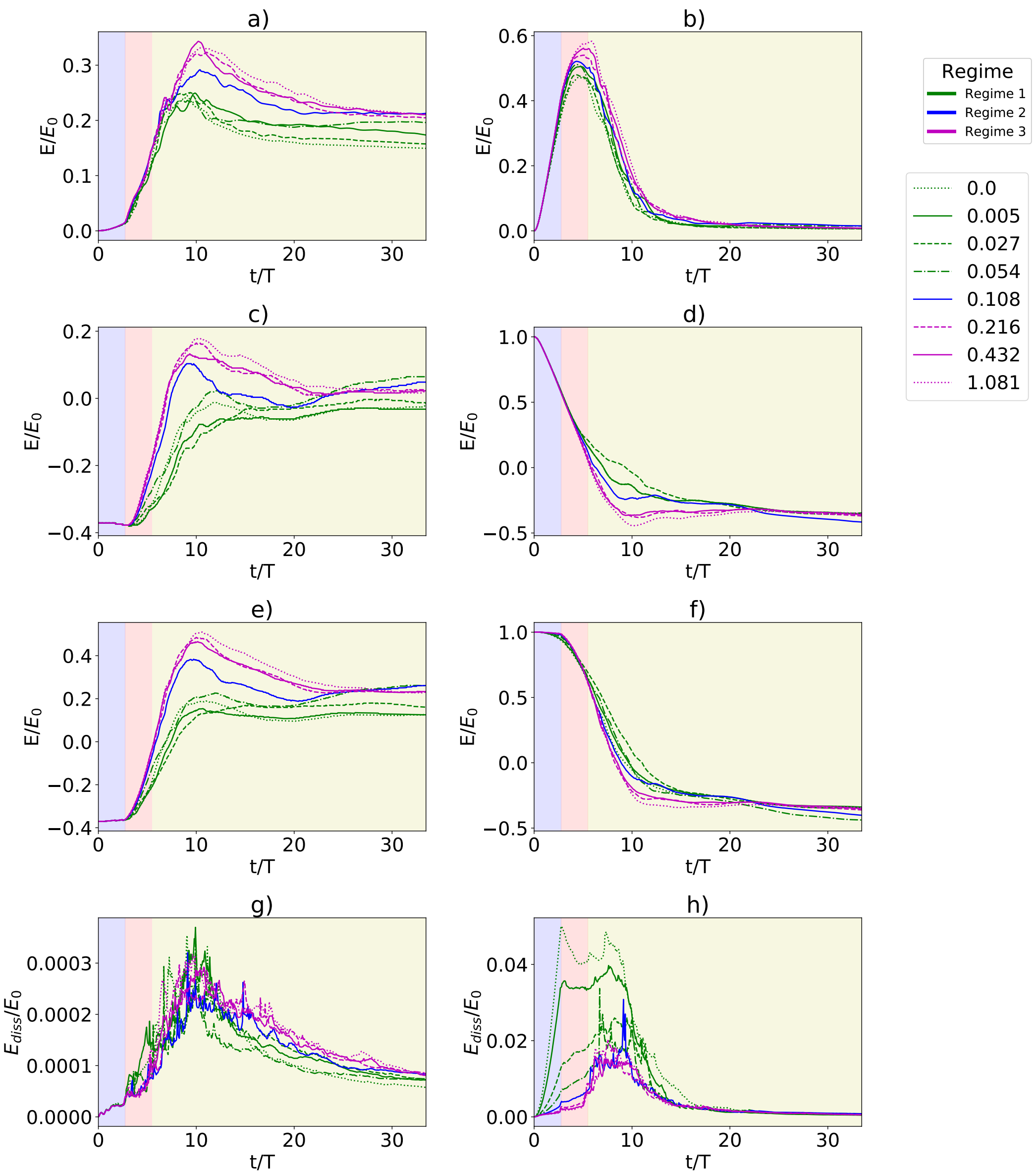

Figure 7. a) Kinetic energy evolution of water. b) Kinetic energy evolution of granular-fluid. c) Potential energy evolution of water. d) Potential energy evolution of granular-fluid. e) Total energy evolution of water. f) Total energy evolution of granular-fluid. g) Dissipation rate of water. h) Dissipation rate of granular-fluid. Results show a range of dimensionless slip lengths, for the initial condition where $\mu = 0.1\ Ns/m^2$ and $H_i = 18.5\ cm$. The plot lines are colored according to the regime they identify with.

rent does not behave in a consistent manner between simulations. For this reason, far field wave gauges are used to reflect the relationship between the slip length and the total energy of the generated wave in the far field, without considering the energy at the interaction or granular-fluid propagation zone (see supplementary material).

With all parameters remaining the same except for the boundary condition, we observe that the boundary condition has a significant impact on the energy available for wave generation, which becomes more profound as the slip is decreased. Not only does the boundary condition influence the energy dissipated in the granular-fluid on the slope, but also the energy dissipated in both the granular-fluid and the water during initial uplift. Due to the complex processes occurring, it is difficult to determine to what extent breaking associated with the different regimes influences the total energy in the far field. As viscosity is decreased, or initial column height is increased, the boundary condition has a less significant impact on the velocity profile of the granular-fluid. Thus, under these conditions, the energy evolutions show far smaller discrepancies.

3.4.2 Effect of boundary condition

Figures 8a-d show the influence of the slip condition and the boundary velocity, on the far-field wave amplitude (considered at $x_1 = 8$m from the shoreline) and maximum total energy of the water. These figures are for the initial conditions $H_0 = 18.5$ cm and $\mu = 0.1$ Nms^{-2}. The first key inference here is that the far field wave amplitude and the maximum total energy of the water follow an almost identical pattern of dependence on slip length. Between $b/H_0 = 0$ and $b/H_0 = 0.2$, there is a sharp increase in both the maximum total energy of the water as well as the far-field amplitude. At b/H_0 > 0.2, this increase becomes more gentle and in one case, a slight decrease in total energy and amplitude is observed. The maximum total energy of the water occurs at t/T ≈ 10, suggesting that most of the initial energy transfer from the granular-fluid to the wave occurs in this time. Plots b) and d) show how maximum amplitude and maximum total energy of the water, respectively, vary with the dimensionless slope boundary velocity. As the boundary velocity increases, it is only once $u_{x,boundary}/u_{x,max} > 0.50$ that we observe a significant increase in energy transferred to the water and likewise, a significant increase in the resulting wave amplitude. This result is surprising, since between $u_{x,boundary}/u_{x,max} >= 0$ and $u_{x,boundary}/u_{x,max} > 0.50$, we expect the largest change in the shape of the boundary layer, and thus energy dissipation. We attribute this to the change in regime; as regime *2* (shearing) becomes closer to regime *3* (plunging), more energy is directed into the total energy of the wave.

Figures 8e and 8f show how the maximum far field amplitude and the maximum total energy of the water relate to the energy lost in the slide, until $t/T = 2.1$. These graphs mirror what is observed in Figures 8b and 8d, showing the velocity on the boundary at impact is correlated to the energy dissipated on the slope before impact. These observations enable us to quantitatively determine the relationship between slip length and energy transfer. For the initial conditions presented, we can infer for a given slip length, what the resulting energy transfer or far-field amplitude would be. Upon changing the initial conditions, if the influence of the slope boundary condition on the granular-fluid velocity profile decreases (i.e. viscosity decreases or column height increases), the same relationships are generally observed, but with less difference between maximum and minimum total energy or amplitude.

The overall energy dissipated in the interaction and wave generation can be a result of viscous friction, air entrainment, mixing processes and the directionality of the granular-fluid front, which influences the amount of of overturning associated with the wave breaking. These observations highlights the importance of exploring the processes occurring at (and before) PDC-water interaction in more detail, in order to capture more accurate initial conditions when performing a numerical hazard assessment and explor-

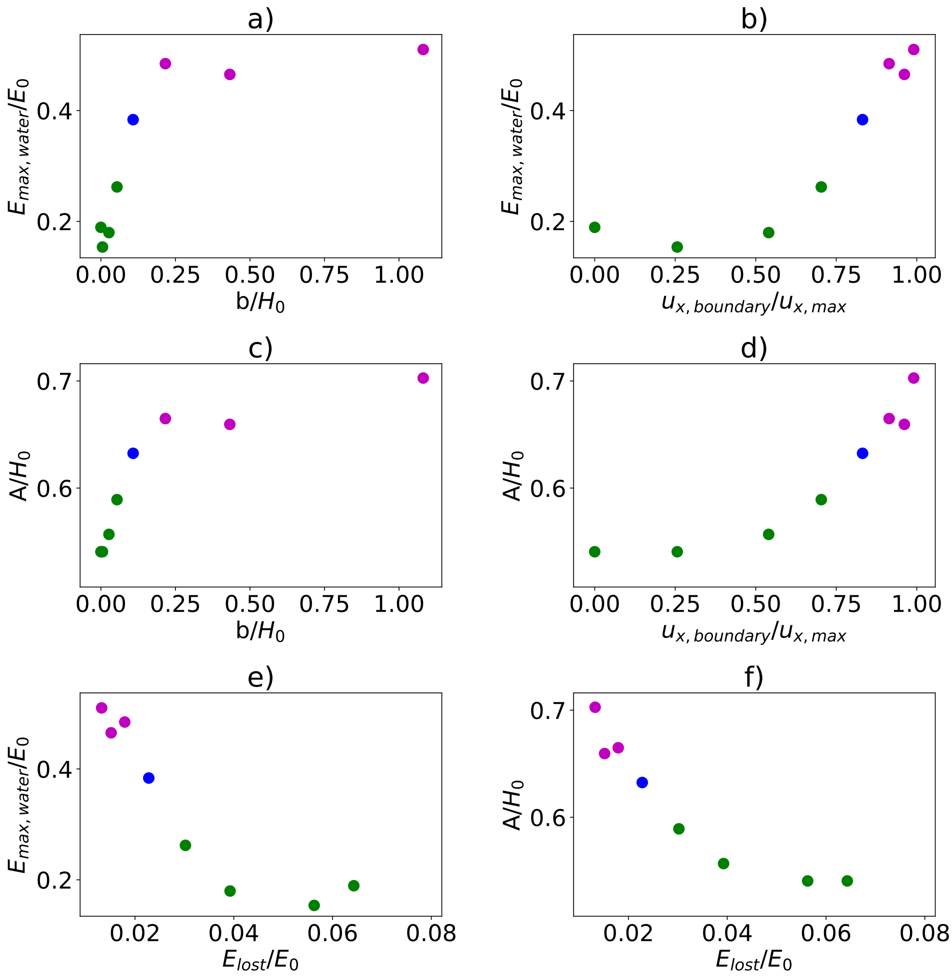

Figure 8. a) Total energy of water variation with slip condition. b) Total energy of water variation with dimensionless boundary velocity at impact $u_{boundary}/u_{max}$. c) Dimensionless far-field (8 m from source) amplitude relative to the slip condition b/H_0. d) Dimensionless far-field amplitude variation with $u_{boundary}/u_{freestream}$. e) Energy lost on the slope before impact (t/T < 2.1, relative to the maximum energy of the water. f) Energy lost on the slope before impact relative to the dimensionless maximum far field wave amplitude. These relationships are for $H_0 = 18.5\ cm$ and $\mu = 0.1\ Nms^{-2}$.

ing a wider range of possible scenarios. Accounting for processes such as mixing at the shoreline might also be a vital step in understanding the characteristics of associated tsunamis.

4 Conclusions

Numerical experiments on the entrance of fluidized granular flows into water have been carried out and compared against laboratory results, in order to explore how the viscosity of the granular-flow and the slope boundary condition play a role in determining the vertical u_x velocity profile of the flow, the associated wave generation mechanism and the far field wave characteristics.

It is shown that the boundary condition of the slope and the granular-fluid viscosity determine to what extent the granular-fluid shears the water surface or propagates down-slope, which has important implications for the wave generation and breaking process. Four key regimes are identified, which describe the different granular-fluid/water interaction styles. These regimes are shown to depend on the slope friction condition b/H_0 and the Froude number of the granular-fluid. For all Froude numbers considered, when friction is significant (i.e. $b/H_0 < 0.01$), the granular-fluid often travels across the water surface causing violent overturning. In some of the high friction cases, however, the granular-fluid initially lifts off then reattaches to the bottom boundary. When reattachment at the shoreline occurs, for lower Froude numbers a low amplitude spilling wave is sometimes generated and a considerable amount of energy is dissipated in the initial shear and reattachment process. For higher Froude numbers, the granular-fluid may reattach, but the majority is directed across the water surface leading to violent overturning. For all Froude numbers, as the friction is reduced, less granular-fluid is redirected across the water surface and a plunging breaker develops. As the boundary condition of the slope tends towards free-slip (this is categorized by $b/H_0 > 0.2$), for $Fr_{granular-fluid}$ < 2.1 a spilling wave is generated. For higher Froude numbers, even for free-slip conditions, a plunging breaker is observed.

Energy dissipation is considered, in order to make inferences about the far-field impact of the different slope boundary conditions and associated interaction regimes. The timing of the different phases of the simulation (e.g. granular-fluid propagation, impact, initial uplift, impact crater collapse and breaking) can be inferred from our outputs and used to form conclusions on how the timings and amount of energy transfer vary across the parameter space. It is concluded that the energy dissipation occurring in the granular-fluid during the first 0.5 s is a significant indicator of the maximum total energy of the water. This relationship is, however, non-linear and as energy dissipation increases, the effect on the maximum energy of the water becomes less significant. The same observation is reflected when considering change in total energy of the water and amplitude with boundary velocity: for the parameters considered, increasing the boundary velocity at impacts makes no significant difference to the energy transfer until $u_{x,boundary}/u_{x,max} > 0.5$. As dynamic viscosity is reduced, or the column height is increased, the impact of the boundary condition on the vertical u_x velocity profile of the granular-fluid becomes less significant and there is less variance in the total energy dissipated.

When considering large scales, these observations may have significant implications for PDC tsunami hazard assessments. Firstly, these experiments validate the assumption that a fluidized granular-flow can be modeled as a viscous Newtonian fluid, particularly in the context of wave generation. Using this assumption, our experiments demonstrate the importance of using an adequate boundary condition for the slope in order to to capture the physics of wave generation and the associated far-field wave characteristics. Our results also highlight the sensitivity of the wave generation process to vertical variations in the horizontal velocity components within the granular-fluid, which is dependent on the relative importance of viscosity. This suggests that exploring the impact of variations in vertical inertia within highly-mobile PDCs may be an important next step when considering large-scale impacts of these flows with seawater. This would require the use of a multi-layer model. Furthermore, our results confirm that denser-than-water, fluidized granular-flows are capable of shearing the water surface and still generating waves of significant amplitude.

Acknowledgments

We would like to acknowledge the University of Auckland Doctoral Scholarship for its generous contribution of PhD fees and stipend of Lily Battershill. The project is also supported by the Marsden Fund Council from Government funding, managed by Royal Society Te Apārangi.

We thank Alexis Bougouin, Raphaël Paris and Olivier Roche for the sharing of their experimental results, including the snapshots presented in Figure 2.

The authors also wish to acknowledge the use of New Zealand eScience Infrastructure (NeSI) high performance computing facilities, consulting support and/or training services as part of this research. New Zealand's national facilities are provided by NeSI and funded jointly by NeSI's collaborator institutions and through the Ministry of Business, Innovation and Employment's Research Infrastructure programme. `https://www.nesi.org.nz`.

The Basilisk code used for the numerical simulations is freely available at `http://basilisk.fr/sandbox/lbattershill/pdc_final/myconserving.h` and `http://basilisk.fr/sandbox/lbattershill/pdc_final/fluidised_flow.c`.

References

Audusse, E. (2005). A multilayer Saint-Venant model: derivation and numerical validation. *Discrete and Continuous Dynamical Systems - Series B*, *5*(2), 189–214. doi: 10.3934/dcdsb.2005.5.189

Báez, W., de Silva, S., Chiodi, A., Bustos, E., Giordano, G., Arnosio, M., … Groppelli, G. (2020). Pulsating flow dynamics of sustained, forced pyroclastic density currents: insights from a facies analysis of the Campo de la Piedra Pómez ignimbrite, southern Puna, Argentina. *Bulletin of Volcanology*, *82*, 1–32.

Baxter, P. J., Boyle, R., Cole, P., Neri, A., Spence, R., & Zuccaro, G. (2005, Apr 01). The impacts of pyroclastic surges on buildings at the eruption of the soufrière hills volcano, montserrat. *Bulletin of Volcanology*, *67*(4), 292–313. Retrieved from `https://doi.org/10.1007/s00445-004-0365-7` doi: 10.1007/s00445-004-0365-7

Bell, J. B., Colella, P., & Glaz, H. M. (1989). A second-order projection method for the incompressible Navier-Stokes equations. *Journal of Computational Physics*, *85*(2), 257–283. doi: 10.1016/0021-9991(89)90151-4

Belousov, A., & Belousova, B. V. (2000). Tsunamis generated by subaquatic volcanic explosions: unique data from 1996 eruption in Karymskoye Lake, Kamchatka, Russia. *Pure and Applied Geophysics*, *157*(6-8), 1135–1143. doi: 10.1007/s000240050021

Belousov, A., Voight, B., & Belousova, M. (2007). Directed blasts and blast-generated pyroclastic density currents: a comparison of the Bezymianny 1956, Mount St Helens 1980, and Soufrière Hills, Montserrat 1997 eruptions and deposits. *Bulletin of Volcanology*, *69*(7), 701–740.

Bougouin, A., Paris, R., & Roche, O. (2020). Impact of fluidized granular flows into water: implications for tsunamis generated by pyroclastic flows. *Journal of Geophysical Research: Solid Earth*, *125*(5). doi: 10.1029/2019jb018954

Branney, M. J., & Kokelaar, B. P. (2005). Pyroclastic density currents and the sedimentation of ignimbrites: Geological Society memoir. *The Journal of Geology*, *113*(1), 115–116. doi: 10.1086/427850

Breard, E., Dufek, J., Fullard, L., & Carrara, A. (2020). The basal friction coefficient of granular flows with and without excess pore pressure: Implications for pyroclastic density currents, water-rich debris flows, and rock and submarine avalanches. *Journal of Geophysical Research: Solid Earth*, *125*(12). doi: 10.1029/2020jb020203

Carey, S., Sigurdsson, H., Mandeville, C., & Bronto, S. (1996). Pyroclastic flows and surges over water: an example from the 1883 Krakatau eruption. *Bulletin of Volcanology*, *57*(7), 493. doi: 10.1007/s004450050108

Cas, R. A., Wright, H. M., Folkes, C. B., Lesti, C., Porreca, M., Giordano, G., & Viramonte, J. G. (2011). The flow dynamics of an extremely large volume pyroclastic flow, the 2.08-Ma Cerro Galán Ignimbrite, NW Argentina, and comparison with other flow types. *Bulletin of Volcanology*, *73*(10), 1583–1609. doi: 10.1007/s00445-011-0564-y

Cas, R. A., & Wright, J. V. (1991). Subaqueous pyroclastic flows and ignimbrites: an assessment. *Bulletin of Volcanology*. doi: 10.1007/BF00280227

Center, N. G. D. (2006, Jul). *Ngdc/wds global historical tsunami database.* U.S. Department of Commerce. Retrieved from `https://www.ngdc.noaa.gov/hazard/tsu_db.shtml`

Deike, L., Popinet, S., & Melville, W. (2015). Capillary effects on wave breaking. *Journal of Fluid Mechanics*, *769*, 541–569. doi: 10.1017/jfm.2015.103

Dufek, J. (2016). The fluid mechanics of pyroclastic density currents. *Annual Review of Fluid Mechanics*. doi: 10.1146/annurev-fluid-122414-034252

Dufek, J., Ongaro, T. E., & Roche, O. (2015). Pyroclastic density currents. *The Encyclopedia of Volcanoes*, 617–629. doi: 10.1016/b978-0-12-385938-9.00035-3

Egorov, Y. (2007). Tsunami wave generation by the eruption of underwater volcano. *Natural Hazards and Earth System Science*. doi: 10.5194/nhess-7-65-2007

Fisher, R. V. (1979). Models for pyroclastic surges and pyroclastic flows. *Journal of Volcanology and Geothermal Research*, *6*(3-4), 305–318. doi: 10.1016/0377-0273(79)90008-8

Freundt, A. (2003). Entrance of hot pyroclastic flows into the sea: experimental observations. *Bulletin of Volcanology*, *65*(2), 144–164. doi: 10.1007/s00445-002-0250-1

Fritz, H. M., Hager, W. H., & Minor, H.-E. (2003). Landslide generated impulse waves: hydrodynamic impact craters. *Experiments in Fluids*, *35*(6), 520–532. doi: 10.1007/s00348-003-0660-7

Giachetti, T., Paris, R., Kelfoun, K., & Ontowirjo, B. (2012). Tsunami hazard related to a flank collapse of Anak Krakatau Volcano, Sunda Strait, Indonesia. *Geological Society, London, Special Publications*. doi: 10.1144/SP361.7

Heller, V. (2009). Landslide generated impulse waves experimental results. *Coastal Engineering 2008*. doi: 10.1142/9789814277426_0109

Hirt, C., & Nichols, B. (1981). Volume of fluid (VOF) method for the dynamics of free boundaries. *Journal of Computational Physics*, *39*(1), 201–225. doi: 10.1016/0021-9991(81)90145-5

Joubert, N., Gardin, P., Zaleski, S., & Popinet, S. (2020). Modelling of mass transfer in a steelmaking ladle. In *Cfd 2020.*

Jutzeler, M., Manga, M., White, J., Talling, P., Proussevitch, A., Watt, S., … Ishizuka, O. (2017). Submarine deposits from pumiceous pyroclastic density currents traveling over water: An outstanding example from offshore Montserrat (IODP 340). *GSA Bulletin*, *129*(3-4), 392–414.

Lagrée, P.-Y., Staron, L., & Popinet, S. (2011). The granular column collapse as a continuum: validity of a two-dimensional Navier–Stokes model with a Mu(I)-rheology. *Journal of Fluid Mechanics*, *686*, 378–408. doi: 10.1017/jfm.2011.335

Legros, F., & Druitt, T. (2000). On the emplacement of ignimbrite in shallow-marine environments. *Journal of Volcanology and Geothermal Research*, *95*(1-4), 9–22. doi: 10.1016/s0377-0273(99)00116-x

Lube, G., Breard, E., Esposti-Ongaro, T., Dufek, J., & Brand, B. (2020). Multiphase flow behaviour and hazard prediction of pyroclastic density currents. *Nature Reviews Earth and Environment*, *1*(7), 348–365. doi: 10.1038/s43017-020-0064-8

Lube, G., Breard, E., Jones, J., Fullard, L., Dufek, J., Cronin, S. J., & Wang, T. (2019). Generation of air lubrication within pyroclastic density currents. *Nature Geoscience*, *12*(5), 381–386. doi: 10.1038/s41561-019-0338-2

Maeno, F., & Imamura, F. (2011). Tsunami generation by a rapid entrance of pyroclastic flow into the sea during the 1883 Krakatau eruption, Indonesia. *Journal of Geophysical Research: Solid Earth*, *116*(9), 1–24. doi: 10.1029/2011JB008253

Mohammed, F., & Fritz, H. M. (2012). Physical modeling of tsunamis generated by three-dimensional deformable granular landslides. *Journal of Geophysical Research: Oceans*, *117*(C11). doi: 10.1029/2011jc007850

Narcisse, Z., Dunkley, P., Edmonds, M., Herd, R., Talipova, T., Andrey, K., & Nikolkina, I. (2004, 01). Tsunami generated by the volcano eruption on July 12-13, 2003 at Montserrat, Lesser Antilles. *Science of Tsunami Hazards*, *22*.

Nishimura, Y., Nakagawa, M., Kuduon, J., & Wukawa, J. (2000). Timing and Scale of Tsunamis Caused by the 1994 Rabaul Eruption, East New Britain, Papua New Guinea. *Tsunamis Advances in Natural and Technological Hazards Research*, 43–56. doi: 10.1007/1-4020-3331-1_3

Nomikou, P., Druitt, T., Hübscher, C., Mather, T., Paulatto, M., Kalnins, L., ... others (2016). Post-eruptive flooding of santorini caldera and implications for tsunami generation. *Nature communications*, *7*(1), 1–10.

Paris, R. (2015). Source mechanisms of volcanic tsunamis. *Philosophical Transactions of the Royal Society A: Mathematical, Physical and Engineering Sciences*, *373*(2053), 20140380.

Popinet, S. (2003). Gerris: A tree-based adaptive solver for the incompressible Euler equations in complex geometries. *Journal of Computational Physics*, *190*(2), 572–600. doi: 10.1016/S0021-9991(03)00298-5

Popinet, S. (2009). An accurate adaptive solver for surface-tension-driven interfacial flows. *Journal of Computational Physics*, *228*(16), 5838–5866. doi: 10.1016/j.jcp.2009.04.042

Popinet, S. (2015). A quadtree-adaptive multigrid solver for the Serre-Green-Naghdi equations. *Journal of Computational Physics*. doi: 10.1016/j.jcp.2015.09.009

Popinet, S. (2020). A vertically-lagrangian, non-hydrostatic, multilayer model for multiscale free-surface flows. *Journal of Computational Physics*, *418*, 109609. doi: 10.1016/j.jcp.2020.109609

Popinet, S. (2021). Basilisk website. Retrieved from `http://basilisk.fr/`

Robbe-Saule, M., Morize, C., Henaff, R., Bertho, Y., Sauret, A., & Gondret, P. (2020). Experimental investigation of tsunami waves generated by granular collapse into water. *Journal of Fluid Mechanics*, *907*. doi: 10.1017/jfm.2020.807

Scardovelli, R., & Zaleski, S. (1999). Direct numerical simulation of free-surface and interfacial flow. *Annual Review of Fluid Mechanics*, *31*(1), 567–603. doi: 10.1146/annurev.fluid.31.1.567

Schlichting, H., & Gersten, K. (2016). *Boundary-layer theory*. Springer.

Sparks, R., Wilson, L., & Hulme, G. (1978). Theoretical modeling of the generation, movement, and emplacement of pyroclastic flows by column collapse. *Journal of Geophysical Research: Solid Earth*, *83*(B4), 1727–1739.

Sulpizio, R., Dellino, P., Doronzo, D., & Sarocchi, D. (2014). Pyroclastic density currents: state of the art and perspectives. *Journal of Volcanology and Geothermal Research*, *283*, 36–65.

Syamsidik, Benazir, Luthfi, M., Suppasri, A., & Comfort, L. K. (n.d.). the 22 december 2018 mount anak krakatau volcanogenic tsunami on sunda strait coasts, indonesia: tsunami and damage characteristics.

Thoraval, M.-J., Takehara, K., Etoh, T. G., Popinet, S., Ray, P., Josserand, C., ...

Thoroddsen, S. T. (2012). Von Kármán Vortex Street within an Impacting Drop. *Physical Review Letters*, *108*(26). doi: 10.1103/physrevlett.108.264506

Ui, T., Matsuwo, N., Sumita, M., & Fujinawa, A. (1999). Generation of block and ash flows during the 1990–1995 eruption of Unzen Volcano, Japan. *Journal of Volcanology and Geothermal Research*, *89*(1-4), 123–137.

Watts, P. (2003). Theoretical analysis of tsunami generation by pyroclastic flows. *Journal of Geophysical Research*. doi: 10.1029/2002JB002265

Waythomas, C. F., & Watts, P. (2003). Numerical simulation of tsunami generation by pryoclastic flow at Aniakchak Volcano, Alaska. *Geophysical Research Letters*. doi: 10.1029/2003GL017220